X-discontinuity and transition zone structure beneath Hawaii suggests a heterogeneous plume

Matthew Kemp[a], Jennifer Jenkins[b], John Maclennan[b], Sanne Cottaar[b]

[a] *Department of Earth Sciences, University of Oxford, United Kingdom*
[b] *Bullard Laboratories, Department of Earth Sciences, University of Cambridge, United Kingdom*

Abstract

The Hawaiian Island chain in the middle of the Pacific Ocean is a well-studied example of hotspot volcanism caused by an underlying upwelling mantle plume. The thermal and compositional nature of the plume alters the mantle phase transitions, which can be seen in the depth and amplitude of seismic discontinuities. This study utilises > 5000 high quality receiver functions from Hawaiian island stations to detect P-to-s converted phases to image seismic discontinuities between 200 to 800 km depth. Common-conversion point stacks of the data are used to map out lateral variations in converted phase observations, while slowness stacks allow differentiation between true conversions from discontinuities and multiples. We find that the 410 discontinuity is depressed by 20 km throughout our study region, while the main 660 is around average depth throughout most of the area. To the southwest of the Big Island we observe splitting of the 660, with a major peak at 630 km, and a minor peak appearing at 675 km depth. This is inferred to represent the position of the hot plume at depth, with the upper disconti-

Email address: matthew.kemp@univ.ox.ac.uk (Matthew Kemp)

Preprint submitted to EPSL *August 17, 2019*

nuity caused by an olivine phase transition and the lower by a garnet phase transition. In the upper mantle, a discontinuity is found across the region at depths varying between 290 to 350 km. Identifying multiples from this depth confirms the presence of a so-called X-discontinuity. To the east of the Big Island the X-discontinuity lies around 336 km and the associated multiple is particularly coherent and strong in amplitude. Strikingly, the discontinuity around 410 km disappears in this area. Synthetic modelling reveals that such observations can be explained by a silica phase transition from coesite to stishovite, consistent with widespread ponding of silica-saturated material at these depths around the plume. This material could represent eclogite enriched material, which is relatively silica-rich compared to pyrolite, spreading out from the plume to the east as a deep eclogite pool, a hypothesis which is consistent with dynamical models of thermochemical plumes. Therefore these results support the presence of a significant garnet and eclogite component within the Hawaiian mantle plume.

Keywords: Mantle, Discontinuities, Conversions, Hawaii, Eclogite

1. Introduction

The mantle plume hypothesis can account for many key features of the hot spot volcanism that has formed the Hawaiian-Emperor Seamount chain (e.g. Wilson, 1963). Originally, mantle plumes were thought to be purely thermal upwellings, but over the past few decades new evidence suggests that mantle plumes carry a compositional component that is anomalous to the background mantle. For the Hawaiian plume, this evidence comes from geochemical analysis which suggests its basalts have been derived from anomalous mineralogy in its source and contain traces of recycled oceanic crust and marine sediments (e.g. Hofmann and White, 1982; Hauri, 1996; Eiler et al., 1996; Sobolev et al., 2005). Geographical variations in the geochemistry of Hawaiian basalts have been linked to spatial variation in the proportion of non-peridotitic material in the mantle source regions (e.g. Sobolev et al., 2005; Frey et al., 2016; Herzberg, 2010; Weis et al., 2011). The basalts on the southwest end of the Big Island are part of the most recent expression of a chain of volcanoes with a distinctive chemistry that is possibly linked to the enhanced contribution of recycled basaltic material to their source regions (the so-called 'Loa' chain). While basalt in the northeast appears to have a greater contribution from melts of peridotitic mantle (the 'Kea' chain) (Sobolev et al., 2005).

Additionally, global seismic tomography shows the Hawaiian plume is broader in the lower mantle than expected for a purely thermal plume (French and Romanowicz, 2015). The regional seismic tomographic model of Cheng et al. (2015) shows a broad, low velocity zone across the upper mantle, which could be explained by ponding of the plume. At the core-mantle boundary, there is seismic evidence of compositional heterogeneity, which could represent the source or anchor of the Hawaiian plume (e.g. Garnero et al., 2016).

Dynamical models show how a plume composition enriched in recycled eclogite causes ponding of plume material above 410-km, creating a so-called

Deep Eclogitic Pool (DEP, Ballmer et al., 2013, 2015; Dannberg and Sobolev, 2015).

One way to elucidate the thermo-chemical nature of the plume and its dynamics across the upper mantle is to image the mantle's seismic discontinuities. These discontinuities are sharp changes in wave speed caused by changes in mantle material properties. The two main seismic discontinuities are around depths of 410-km and 660-km, and are associated with the phase transition of olivine to wadsleyite (Katsura and Ito, 1989) and dissociation of ringwoodite (Ito and Takahashi, 1989), respectively, in an olivine-dominated mantle. We will refer to these transitions as the 410 and the 660, and the region between them as the Mantle Transition Zone (MTZ).

The olivine phase transitions associated with the 410 and 660 discontinuities have opposite Clapeyron slopes in temperature-pressure space. In hot regions the 410 becomes depressed and the 660 is uplifted, leading to a thin MTZ; in cold regions the 410 is uplifted and the 660 is depressed, leading to a thick MTZ. Therefore, if mantle plumes were purely thermal features, mapping the MTZ thinning beneath a plume could be used as a thermometer for mantle temperature.

However, complications arise around 660-km depth, where, in addition to the olivine phase transition, there is a transition in majorite garnet with an opposite sign, a positive Clapeyron slope (e.g. Hirose, 2002; Liu et al., 2018). The discontinuity caused by this phase transition can dominate the seismic image if garnet is stable (Yu et al., 2011). Garnet stability occurs at higher temperatures or in basalt enriched compositions (e.g. Xu et al., 2008; Stixrude and Lithgow-Bertelloni, 2011). A discontinuity created by this phase transition would be depressed in hot regions. Several seismic studies have observed two discontinuities around 660-km, a so-called splitting of the 660, suggesting both phase transitions are occurring (e.g. Andrews and Deuss, 2008), while other studies observe a single deeper discontinuity in plume regions (e.g. Jenkins et al., 2016).

Previous studies of the Hawaiian region, based either on MTZ thinning or mapping slow velocity zones in tomographic models, show remarkable inconsistency in their estimates of the position of the plume. In terms of P-to-s converted phase studies, some (Li et al., 2000; Shen et al., 2003; Wölbern et al., 2006) find maximum MTZ thinning to the south and southwest of the Big Island, whereas Huckfeldt et al. (2013) find maximum thinning towards the southeast and Agius et al. (2017) find thinning under north-central Hawaii.

Seismic discontinuities that are not observed globally can indicate the presence of compositional heterogeneity. For example, at around 300-km depth in some regions around the globe, a discontinuity - named the X discontinuity - is present. A discontinuity around this depth beneath Hawaii has been observed with ScS reverberations (Courtier et al., 2007) and SS precursors (Deuss and Woodhouse, 2002; Schmerr et al., 2013; Schmerr, 2015). This has been associated with various phenomena, including: a phase transition in silica from coesite to stishovite, a crystallographic change in orthopyroxene, the formation of hydrous phase A - a dense magnesium silicate - or the reaction of forsterite + periclase into anhydrous-phase B. It follows that if the X-discontinuity is detected then this has implications for the composition and dynamics of the mantle.

In this study we image both the MTZ and upper mantle structure beneath Hawaii using over 5000 P-to-s converted phases or receiver functions (RFs). We interpret our observations in relation to mineral physics and geodynamics which further highlights the thermochemical nature of the Hawaiian mantle plume.

2. Data and Methods

2.1. Data Acquisition

Seismic data are obtained from the publicly available IRIS (Incorporated Research Institutions for Seismology) data centre for stations across the Hawaiian Islands. Recordings are selected for stations located between 15°/25° latitude and -165°/-150° longitude during the time period of 1990-2017. Data is collected for events with magnitude (Mw) 5.5-8, at epicentral distances between 30°-90°. This results in over 100,000 recordings from 77 stations across eight networks (Figure 1).

Ocean Bottom Seismometers (OBSs) were deployed around the Hawaiian Islands in the PLUME experiment from 2007-2009 (Laske et al., 2009). However, we find that the data from these stations is excessively noisy. While we do observe significant, but weak, arrivals for the 410 and 660 in the OBS data, including this data decreases our ability to detect generally weaker upper mantle signals, and interpret the observed amplitudes with confidence. Audet (2016) describes the challenges of creating OBS teleseismic receiver functions caused by the water column and marine sediments. For these reasons OBS data is not included in this study.

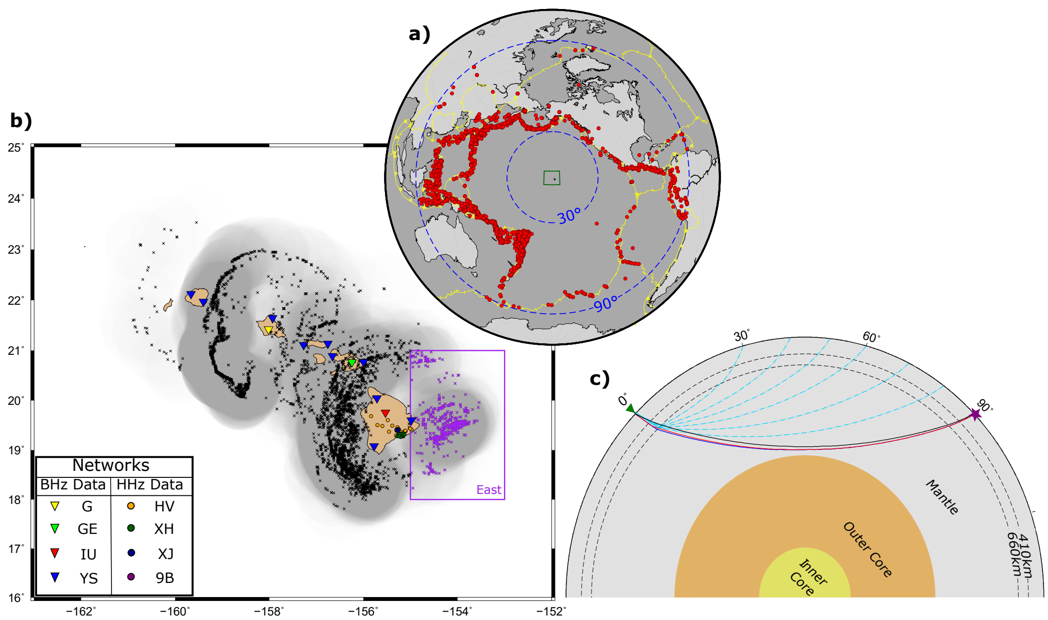

Figure 1: a) Global map showing earthquake epicentres (red circles) of the 5132 high quality RFs, epicentral distances 30° and 90° (blue dashed circles) from the centre of our study region (green square), and plate boundaries (yellow lines). b) Map of study area around the Hawaiian island chain showing seismic stations as inverted triangles (for BHZ data - sample rate 10-80 Hz) and circles (for HHZ data - sample rate 80-250 Hz), coloured by network. Pierce-points for P410s at 410 km are shown by black and purple (for region E) crosses, and half-width Fresnel zones of P410s at 410 km by 99% transparent grey circles. c) Schematic cross-section showing example ray paths of P660s phases at various distances (dashed cyan lines), and one set including the direct P (black), P410s (red) and P660s (blue) from source (pink star) to receiver (green triangle) to illustrate similarity in ray paths. (Adapted from Jenkins et al. (2016) Figures 3 and 4)

2.2. Receiver Functions and Quality Control

When P waves interact with seismic discontinuities, some of the energy can be converted into S waves, producing P-to-s or Pds phases (where d is the depth of the discontinuity in kilometres, e.g.: P410s and P660s). To observe converted phases, which have a relatively low amplitude, data from many events need to be stacked. To do this the source component is deconvolved from the data, creating so-called receiver functions (RFs). These are created by removing the source-time function, instrument response and source side effects from the converted phases, leaving a direct representation of the Earth's structure beneath the receiver along the incoming ray path. The vertical component (Z) of ground motion preferentially records the direct P arrival, which we assume is a good representation of the source signal, and the horizontal radial component (R) preferentially records the Pds converted waves. Initially we cut a time window of 25-seconds before, to 150-seconds after the main P arrival on the Z and R components. The Z component is then deconvolved from the R component using the Iterative Time Domain Deconvolution Method (Ligorra and Ammon, 1999) (Figure 2a).

Iterative Deconvolution uses Gaussian pulses to construct RFs in the time domain. Starting with an empty RF trace, we iterate between evaluating the misfit between the convolved RF and vertical component, and the radial component, adding a Gaussian peak where the misfit is largest (scaled by the misfit amplitude). The iteration stops when the misfit improves less than 0.01% or when 200 peaks are added. Here we construct two sets of RFs using a 'wide' Gaussian half-width of 2.5-s and a 'narrow' Gaussian half-width of 1.0-s. We refer to the two cases as 'low-frequency' and 'high-frequency' RFs. For both cases the data are pre-filtered using high-pass filter of 0.01 Hz and a Gaussian filter related to the Gaussian peak width, respectively. The vertical resolution of the low- and high-frequency RFs are around 23-km and 9-km, respectively, around 300-km depth, illustrating the importance of the high-frequency RFs to distinguish nearby multiples and split arrivals (even though amplitudes are weaker for high-frequency RFs).

Automatic and manual quality checks are applied to the RFs, removing over 90% of the traces. Details are given in Supplementary Section 1.1.

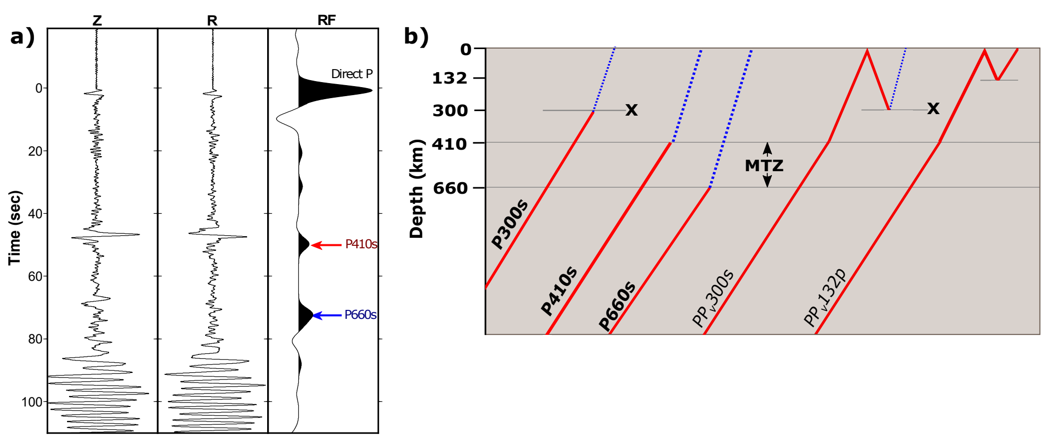

Figure 2: a) Examples of vertical (Z) and radial (R) components of ground motion for an event recorded at IRIS station KIP in Hawaii and the resulting RF obtained by deconvolving the vertical from the radial components (a 'low-frequency' RF). Direct P (black), P410s (red) and P660s (blue) phase arrivals indicated on the RF. b) Ray paths of P-to-s converted phases this study focuses on (labelled in bold in the form Pds where d is the depth of conversion) and surface multiples (labelled in italic in the form PPvds or PPvdp, where v denotes a topside reflection). P waves - solid red line, S waves - dotted blue line. (Adapted from Jenkins et al. (2017) Figure 3)

2.3. Stacking Methods and Time to Depth Conversion

The amplitude of the coherent Pds converted phases are small compared to the incoherent noise. Stacking the RFs (using a variety of methods) increases the signal-to-noise ratio, enhancing the Pds arrivals.

Some stacking methods are applied in the depth domain, requiring RFs to first be converted from time to depth. The RFs are converted using a combination of the crustal model, Crust1.0 (Laske et al., 2013) and the regional tomographic model of Cheng et al. (2015), which gives regional relative shear wave velocities with no fixed 1D reference model. The relative velocities are given to an unknown mean absolute velocity, which in the Hawaiian case is probably slower than the global mean, causing spurious fast anomalies around the plume in the Cheng et al. (2015) tomographic model (Bastow, 2012). To subdue this issue, we shift to relative velocities 0.5% slower before converting to absolute velocities, using the 1D PREM (Dziewonski and Anderson, 1981). Using these conversions puts the 660 discontinuity at approximately global averaged depths. The relative P wave velocities are scaled down by a factor 2 at the top, linear increasing to 2.35 at 1000 km. For each depth, the predicted Pds - P differential time and conversion point for the Pds ray path are computed by back-tracing from the station towards the event. We account for the 3D velocities in the station-event plane, but use a 1D predicted incident angle at the station to start tracing the ray.

We show results for three different stacking techniques. 'Depth' and 'common conversion point (CCP)' stacks are used to identify the depth and location of conversions, while 'slowness' stacks are used to identify if arrivals are converted phases from depth or are surface multiples.

- Depth stacking (Figures 3a,c and 6a,c): RFs are averaged together in the depth domain for the entire study region as well as a subset of data sampling a region to the East of the Big Island ('region E', defined in Figure 1b). Each peak represents an arrival which could be a Pds converted phase, or a multiple. If the peak is found to be a converted phase, then the depth of the maxima represents the conversion depth and hence the discontinuity depth.

- Common Conversion Point (CCP) stacking (Figure 5): A 3-dimensional volume beneath Hawaii is discretized every 0.2-degrees in latitude and longitude and 2-km in depth. For each grid point the horizontal distance to each RF's predicted Pds conversion pierce point within the 3D model is computed. The amplitude of the RF at that point is added to the grid point multiplied by a weighting factor dependent on the ratio of the distance and the Fresnel zone half-width for a 10-s S wave at the given depth (i.e. 116-km for P410s phase at 410-km and 162-km for P660s phase at 660-km). The weighting factor introduces smoothing by reducing to zero at twice the Fresnel zone half-width along a normalized cubic spline (see details in Cottaar and Deuss, 2016). We also track the standard error at each grid point using the difference of the RF amplitude with the running average. We show amplitudes above twice the standard error in plotted cross-sections. Discontinuity topography maps (Figure 4) are extracted by picking and interpolating the maximum amplitude peaks found within a specified depth range.

- Slowness stacking (Figures 3b,d and 6b,d): Energy from surface multiples can interfere with conversions as they arrive at similar times (possible interfering phases are shown in Figure 2b). Slowness stacks are used to distinguish between them, as conversions come in with negative slowness relative to the direct P wave (equivalent to a steeper incoming angle), while surface multiples come in with positive slowness relative to the direct P wave (or shallower incoming angle). These stacks are created by shifting all the RFs in time to a common epicentral distance of 60° using relative slowness values between 1 and -1 compared to the direct P wave slowness, and then stacking the shifted RFs for each of these slowness values. A 'bullseye' pattern shows positive and negative coherent amplitude arrivals in slowness-time space (the term 'bullseye' is used to indicate a peak in coherent amplitude throughout this study even if it appears streaked). Predicted lines and positions in slowness-time space for predicted Pds converted phases and multiples are computed for PREM (Dziewonski and Anderson, 1981) and shown for reference. Note that at earlier times, and therefore increasingly at shallower depths, the predicted lines for phases converge, making it harder to distinguish between conversions and multiples.

2.4. Synthetics

To test interpretations of the observations, synthetic data are computed using reflectivity synthetics (CRFL, Fuchs and Müller, 1971). The processing of the synthetics largely follows the same procedure as the observations, and further details are given in Supplementary Section 1.2.

3. Results

We image the upper mantle and Mantle Transition Zone (MTZ) structure using 5132 high quality RFs around the Hawaiian islands. We first create depth and slowness stacks of the entire dataset to show the average depths of possible discontinuities across the region. The full dataset low-frequency depth stack (Figure 3a) shows four clear peaks above error at depths of 167, 289, 434 and 656 km. We use the slowness stack (Figure 3b) to discern whether these peaks are true converted phases from depth or multiples. The bullseyes for the 434 km and 656 km arrive at correct slownesses to be depth converted phases. Both stacks confirm that on average the 410 is deeper (at an average of 434 km) while the 660 is only slightly shallower than expected. The MTZ thickness is on average 222 km, significantly thinner than the global average of 242.0-250.8 km (Lawrence and Shearer, 2006; Andrews and Deuss, 2008). Discussion on the lack of an observation around 520 km can be found in Supplementary Section 2.1.

For arrivals in the upper mantle it is more difficult to distinguish the slownesses of direct arrivals and multiples. The bullseyes in the slowness stack at lower frequency (Figure 3b) corresponding to the arrivals at 167 and 289 km are of too limited resolution in the slowness domain to unequivocally say they are arrivals from depth. Analysing the higher frequency stacks (Figure 3c and d) helps to further distinguish between conversions and multiples. In Figure 3d, there are two clear bullseyes on the slowness stack that correspond to peaks around 300 km in the depth stack: one strong arrival centred around the predicted multiple lines, and one weaker arrival on the direct conversion line. This indicates that a P300s likely interferes with a multiple generated from shallower structure, which could be the PPv132p, PPv84s or PSv68s. PPv132p is the closest predicted phase in both time and slowness to observations and could result from the positive velocity jump seen around 110-155 km beneath Hawaii in previous studies (Rychert et al., 2013). Further evidence for the presence of a discontinuity around 300 km is a bullseye (relative amplitude of 1.4%) arriving 90-100 seconds in the slowness stack. This is very close to the predicted position for a PPv300s multiple, providing further evidence that there is indeed a discontinuity around 300 km. Hereafter we will refer to this feature as the X-discontinuity (Schmerr, 2015) and the related phases PXs and PPvXs. The X-discontinuity has a variable appearance across the region, and is difficult to observe due to incoming multiples from shallower structure, thus we could not produce a clear map of X-discontinuity topography.

The bullseye for the arrival at 167 km is too shallow to distinguish between the conversion and multiple line and there are no clear multiples coming from this depth. For these reasons it is not investigated further in this study.

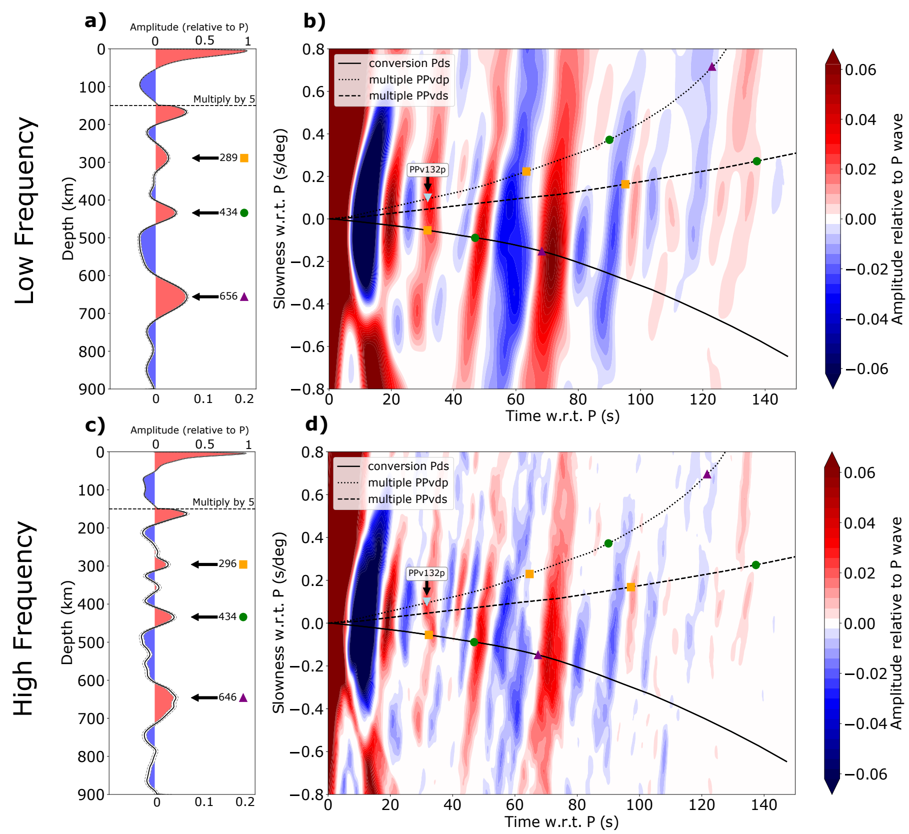

Figure 3: Depth (a and c) and slowness (b and d) stacks of all 5132 RFs used in this study at ‘low-frequency’ in a and b and ‘high-frequency’ in c and d. Depth stacks (a and c): The average amplitude at depth (solid black line) is plotted along with the lines reflecting 2 Standard Error (dashed black line). Arrows indicate the significant positive peaks, with the depth in kilometres and individual symbols. Beneath 150 km the stack is multiplied by 5 to bring out the lower amplitude peaks. Slowness stacks (b and d): Relative amplitudes (>2 SE) shown as a function of time and slowness. Predicted lines for the conversion and multiple phases in slowness/time space using PREM are shown as: Pds (direct conversion) - solid line, PPvds (multiple) - dashed line, PPvdp (multiple) - dotted line. The symbols indicate predicted arrivals for the corresponding peaks in the depth stacks : 289/296 km - orange square, 434/434 km - green circle, 656/646 km - purple triangle for the low/high-frequency stacks. The predicted PPv132s phase is indicated with an light blue upturned triangle; this is the predicted phase that interferes with PXs. Note that the depth stacks use a 3D model to convert from time to depth, while the predictions for the slowness stack use 1D PREM.

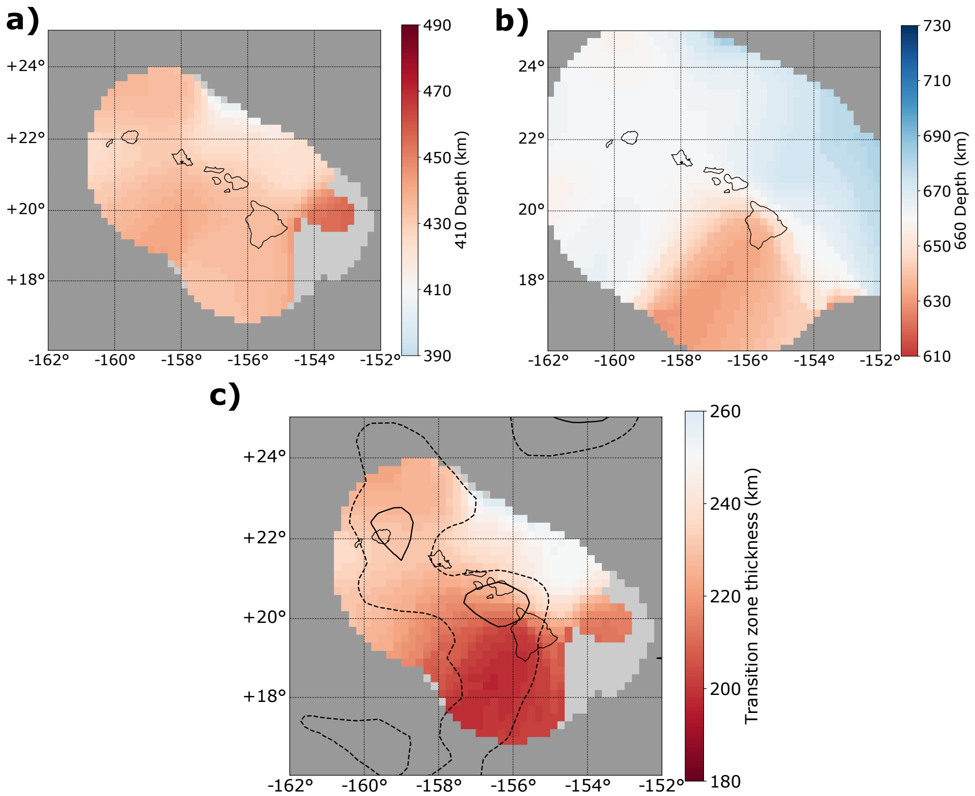

Figure 4: a) Map of topography of significant 410 arrivals from the low-frequency CCP stack. 410 km is defined as white and shallower regions are blue, deeper red. b) Map of topography of significant 660 arrivals. 660 km is defined as white and shallower regions are red, deeper blue (opposite from 410 to reflect the opposite Clapeyron slope commonly associated with 660). c) Map of MTZ thickness, i.e. the difference between a and b. 250 km is defined as white, thinner is red and thicker is blue. Contours of a slice at 410 km through the Cheng et al. (2015) regional tomographic model shown as solid (-2%) and dashed (-1%) black lines. In all three plots dark grey represents no data and light grey represents points where no significant positive arrival is observed within the depth range.

3.1. MTZ thinning southwest of the Big Island

Depths for significant peaks around 410 km (Figure 4a) and 660 km (Figure 4b) are extracted from our regional CCP stack and the difference is plotted as a map of MTZ thickness (Figure 4c). The 410 appears deep across

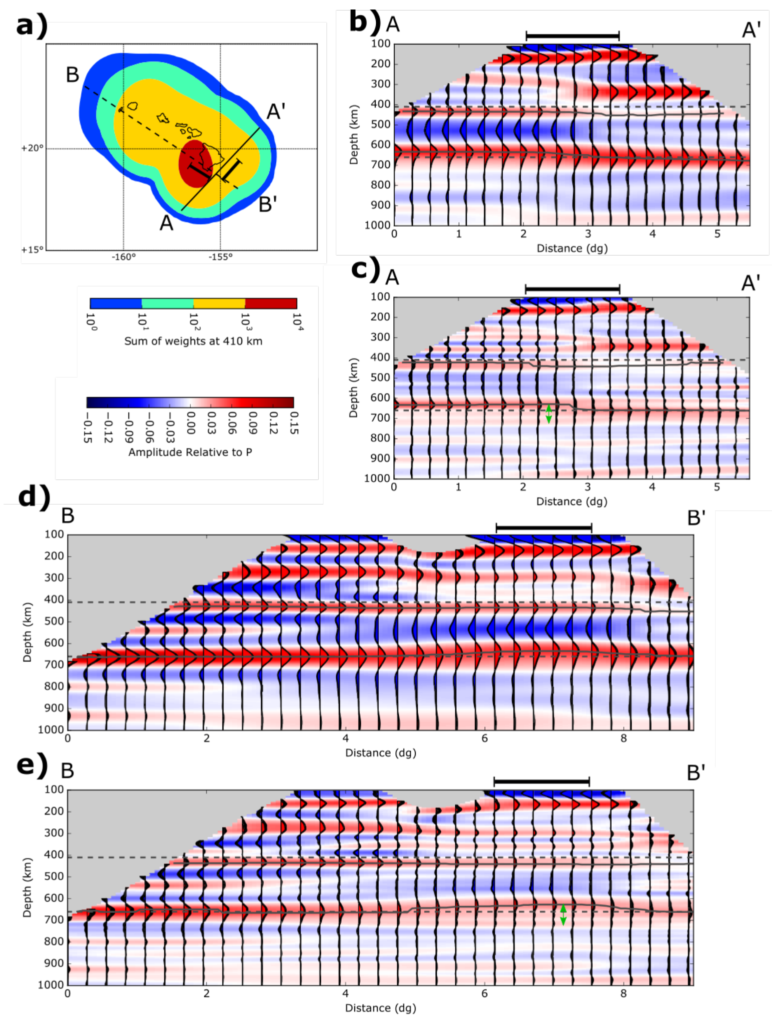

Figure 5: Cross-sections of CCP stacks. Grey is regions where the sum of the weights is less than 50. The two cross-sections run from SW-NE (A-A′) b-c and from NW-SE (B-B′) d-e. a) The map of Hawaii shows the summed weights in the CCP stack at 410 km depth and cross-section lines (A-A′ solid and B-B′ dashed). The background and regularly spaced profiles are interpolated from the CCP grid and show red for positive and blue for negative peaks (>2 SE). The grey dashed lines mark out 410 and 660 km depths and solid grey lines track the observed peaks around 410 and 660 km. b and d are stacks for low-frequency RFs, c and e are stacks for high-frequency RFs. A black bar above each cross-section indicates the position of the Big Island. Green double-headed arrows (in c and e) indicate the peak-splitting at ∼660 km.

the entire area. The MTZ thickness map shows the thinnest MTZ of 200 km occurs to the southwest of the Big Island, $\sim$50 km thinner than the global average (Lawrence and Shearer, 2006), mainly due to uplifting of the 660 to $\sim$630 km.

Figure 5 shows cross-sections through CCP stacks from southwest to northeast of the Big Island (A-A′) and northwest to southeast of the Big Island (B-B′). B-B′ (Figure 5d,e) shows the transition from the more average TZ in the northwest, with a deep 410, to the anomalous TZ in the southwest, with a shallow 660. The cross-section shows that the 660 also becomes wider and more diffuse (Figure 5d). In the high-frequency cross-section (Figure 5e) this diffuse 660 splits into two distinct peaks, one that upwells and the other lower amplitude peak that slightly deepens. In the lower frequency CCP stacks, the shallower larger amplitude 660 peak controls the observed discontinuity topography in Figure 4b.

The deepening of the 410 across the area suggests it is affected by a widespread thermal anomaly above the 410, while the 660 is only locally affected. However, this image can depend on how we apply the time-to-depth conversion. We use the relative velocity model of Cheng et al. (2015) shifted slower by 0.5% and converted to absolute velocities using PREM. Compared to a CCP stack using the 1D PREM for time-to-depth conversion, the 3D model shifts the average 410 depth 10.0 km shallower and the average 660 depth 17.24 km shallower. Instead, if we were to shift the velocities even slower (suggesting the velocity anomalies associated with the mantle plume are under-resolved or the background mean is slower than our assumption), two alternative scenarios can be created. In the first scenario, using a negative velocity shift both discontinuities would move upwards. In this case, the 660 is shallower and the 410 only slightly deeper than global averages and the thermo(-chemical) anomaly would be interpreted to affect both phase transitions across the whole imaged region. In the second scenario, if the velocity model were shifted even slower, the discontinuities become even shallower, causing an uplift of the 660 by 20-30 km and a 410 appearing at average global depth. This scenario suggests an anomaly that only affects the 660 discontinuity which could be explained by widespread ponding of hot plume material or a harzburgitic component (Yu et al., 2018) beneath the 660. Here we favour the interpretation of a widespread temperature anomaly above the MTZ affecting the depth of the 410, produced with the Cheng et al. (2015) model shifted slower by only 0.5%, as the most realistic scenario. We discuss the the potential cause of such an anomaly in Section 4.

3.2. Anomalous Eastern Region

Cross-section A-A′ in Figure 5b,c shows the transition between the southwest of the Big Island and region to the East. The 660, which is anomalous to the southwest, appears at an average depth to the east, where the 410 arrival weakens in amplitude.

Figure 6 shows separate depth and slowness stacks for the region to the east of the Big Island, hereafter named region E (location shown in Figure

1). The most striking observation for region E, is a very weak arrival from the 410, which falls below the 2 standard error significance level in the high-frequency stacks (Figures 6c and d).

Region E also shows a strong amplitude X-discontinuity. We note the direct arrival of the X-discontinuity again interferes with a multiple (potentially the PPv163p phase). The X-discontinuity's multiple (PPvXs) however, appears as a more coherent arrival compared to the entire region (Figure 3b) and has an average relative amplitude of 2.0% across both filters. As well as being particularly strong in amplitude here, the X-discontinuity is also slightly deeper (336 km) than the regional average (296 km, Figure 3b). This deepening is seen as a delay to the PXs arrival (from 35 to 40 seconds) and a corresponding delay for the PPvXs multiple (from 108 to 113 seconds). An artefact of the multiple is also observed in the cross-sections around 900-1000 km (Figure 5), mirroring the topography seen on the shallower X-discontinuity arrival. We note that there appears to be a strong negative arrival before the positive arrival of the X-discontinuity in these stacks, with suggestions of a corresponding negative multiple.

In the Supplementary Section 2.2, we show how the variation in MTZ around the Big Island can be illustrated by stacking by back-azimuth of incoming events.

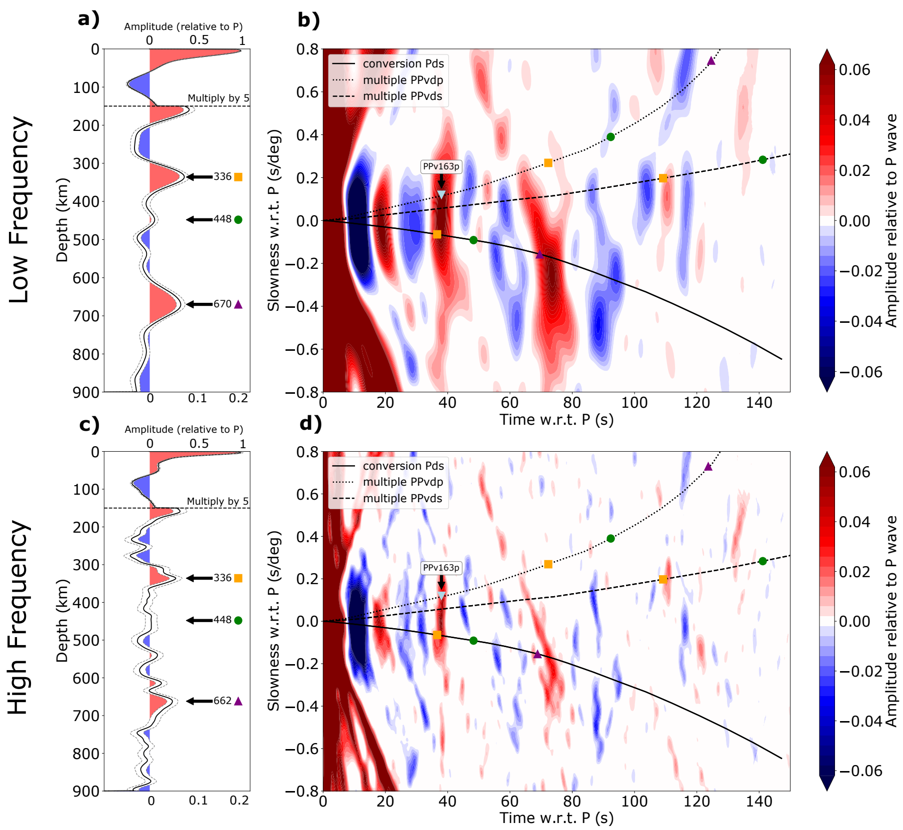

Figure 6: Depth (a and c) and slowness (b and d) stacks of low-frequency (a and b) and high-frequency (c and d) RFs for the 594 RFs to the East of the Big Island (region E, see Figure 1). See Figure 3 for explanation of the different stacks, lines and markers. PPv163p indicated as possible phase interfering with PXs.

4. Discussion

This study maps converted phases from the upper mantle and MTZ beneath the Hawaiian Islands. Notable observations include a significantly thinned MTZ to the SW of the Big Island combined with an observation of a double peak on the 660 in the area of maximum thinning. The X-discontinuity is observed throughout the region and appears particularly strong towards the E of the Big Island, where the 410 conversion almost disappears. Here we interpret the appearance and form of these discontinuities in terms of potential thermal and compositional properties of mantle material.

4.1. Plume signature across the transition zone

4.1.1. Discontinuity topography

The 410 appears deep across the area of study by about 20 km, leading to generally thinned MTZ. To the SW of the Hawaiian Big Island, there is an area that has an even thinner MTZ than the average for Hawaii, ~50 km thinner than the global average. The additional thinning is mainly due to the 660 in this area shallowing to ~630 km. We interpret this to be the position of the upwelling mantle plume across the MTZ.

The plume location based on the 410 topography is less clear, as its depression is quite consistent, suggesting a potential widespread thermal anomaly affects the 410. The interpretation of a widespread thermal anomaly above the 410 correlates with widespread low shear velocities at the bottom of the upper mantle in the velocity model of Cheng et al. (2015). We will discuss further in Section 4.2 how this interpretation is also supported by our observation of the X-discontinuity and the missing 410, as well as results from recent geodynamic modelling. Temperature estimates based on the discontinuity topography are discussed in Supplementary Section 2.3.

The regional tomographic model of Cheng et al. (2015), shows a $< -2\%$

velocity structure to the NW of the Hawaiian islands at around 400 km depth (Figure 4c), further north than where our study predicts the plume position. The location of the plume to the SW of the Big Island is consistent with multiple other P-to-s conversion studies (Li et al., 2000; Shen et al., 2003; Wölbern et al., 2006). However, more recent P-to-s studies come to different conclusions. Huckfeldt et al. (2013) finds the strongest thinning towards the southeast, while Agius et al. (2017) finds thinning of 13 km under north-central Hawaii. The study of Huckfeldt et al. (2013) also observes a deep 410 across the region, while in Agius et al. (2017) both the 410 and 660 are at average depths. There are clearly large discrepancies in predicted plume location between studies. However we are confident in our interpretation that the plume stem is located SW of the Big Island, due to the additional observation of a split 660 in this region.

4.1.2. A double peak at 660 km

The splitting of the 660 in the SW region offers possible insights into both thermal and compositional heterogeneities in the mantle. In the high-frequency cross-section of the CCP stack (Fig 5e), the SW region shows two peaks at around 660 km: one that appears shallower (by $\sim$30 km) and one that appears deeper (by $\sim$50 km). The upper peak is likely to correspond to the dissociation of ringwoodite to bridgmanite and magnesiowstite. The deeper peak appears to have the opposite Clapeyron slope, becoming deeper as the upper peak shallows. We interpret this to represent a discontinuity caused by the phase transition of majorite garnet to bridgmanite that also is predicted to occur around this depth at relatively higher temperatures, and has a positive Clapeyron slope (Liu et al., 2018). If this is the case the location of the split at 660 represents the location of highest temperature anomaly, further supporting our interpretation of the plume being located to the SW of the Big Island.

The garnet transition is generally predicted to be more gradational with depth than the ringwoodite transition as majorite garnet can co-exist with bridgmanite over a large range of pressures and temperatures (e.g. Yu et al., 2011). Additionally, compositional effects from inclusion of mafic components, such as recycled basalt, would broaden the majorite stability field (Xu et al., 2008). This could explain the smaller amplitudes of the deeper of the two peaks we observe, since broader discontinuities produce lower amplitude converted arrivals.

The presence of both phase transitions occurring together is predicted to happen over a very specific temperature range, approximately 200–300 K above global average (Hirose, 2002; Stixrude and Lithgow-Bertelloni, 2011). The garnet-controlled phase transition has been suggested to dominate observations of depressed 660 topography beneath Iceland (Jenkins et al., 2016), where the olivine-controlled phase transition is not observed. This could indicate that Icelandic plume stem is hotter and/or carries more garnet than the Hawaiian plume.

4.2. Heterogeneous signals in the upper mantle: X-discontinuity

4.2.1. Comparison to previous observations

Various studies have reported the presence of the X-discontinuity beneath the Pacific and specifically Hawaii using ScS reverberations (Courtier et al., 2007) and SS precursors (Deuss and Woodhouse, 2002; Schmerr et al., 2013; Schmerr, 2015). Schmerr (2015) observes the X-discontinuity across the Pacific at 293 $\pm$ 65 km which is consistent with our observations. SS precursor bounce points have much broader coverage across the Pacific, but also average over an order of magnitude wider Fresnel zone compared to RFs (1000s km for precursors versus 100s km for RFs). Schmerr (2015) observes a weak ($< 2\%$ impedance contrast) presence of the X-discontinuity beneath Hawaii; this could be due to strong topography on the discontinuity causing incoherent reflections and stacking.

4.2.2. Proposed causes

Various mineral and physical processes have been proposed to explain the X-discontinuity, but these hypotheses do not always apply to mantle plume settings:

- Formation of hydrous phase A - a dense magnesium silicate - (e.g. Akaogi and Akimoto, 1980): Stability of this phase requires relatively low temperatures and high water content conditions as found in subduction zone settings.

- The reaction of forsterite + periclase into Anhydrous-phase B: This mechanism requires substantial periclase enrichment (Chen et al., 2015), which could occur in hydrated mantle/subduction zone settings (Ganguly and Frost, 2006).

- A crystallographic transition in pyroxene (clinoenstatite) from orthorhombic to monoclinic structure (Woodland, 1998): This transition has a strong positive Clapeyron slope and a weak impedance contrast($< 2\%$), which further weakens at higher temperatures (e.g. Xu et al., 2008; Schmerr, 2015), making its visibility unlikely.

- A phase transition in silica from coesite to stishovite with a positive Clapeyron slope (e.g. Akaogi et al., 1995): These silica phases are expected to be present in mafic material with basaltic bulk compositions, potentially brought up in mantle plumes.

From here on we will explore the potential for the coesite-stishovite phase transition to explain our observations. This model can account for precursor observations of the X-discontinuity across the broader Pacific (Schmerr, 2015), and is consistent with a high-temperature plume setting. The presence of this transition is easier to invoke in regions where basalt is subducted (Williams and Revenaugh, 2005), but recycled oceanic basalt has been suggested to be present in the Hawaiian plume (Hofmann and White, 1982; Sobolev et al., 2005; Herzberg, 2010).

4.2.3. Coesite-stishovite transition

Average mantle is thought to have a pyrolitic composition (McDonough and Sun, 1995), which contains a large modal proportion of olivine at low pressure, leading to the generation of the globally observed olivine-wadsleyite and ringwoodite-bridgmanite+magnesiowstite phase transitions at 410 and 660 km depth respectively (Katsura and Ito, 1989; Ito and Takahashi, 1989). No silica phases are present in a pyrolitic composition, and therefore we do not expect a globally observed seismic discontinuity at the predicted depth of 300 km. However, the presence of unequilibrated mafic material, in a mechanical mixture of different compositions, allows for the presence of silica phases (e.g. Xu et al., 2008). A possible source of such compositional heterogeneity is from the presence of recycled basaltic material in the plume source. Recycled basalt compositions are expected to be stable as an eclogite containing pyroxene, garnet and a free silica phase in the P-T conditions of the upper mantle under Hawaii (Jennings and Holland, 2015). Compositional characteristics of Hawaiian basalts have been linked to the presence of recycled material in their mantle source regions (e.g. Hauri, 1996; Eiler et al., 1996; Frey et al., 2016). The major element compositions of the Loa-trend of volcanoes provide some of the strongest evidence for the presence of recycled basalt (e.g. Sobolev et al., 2005; Herzberg, 2010).

The strong impedance contrast of the co-st transition indicates that only a small % of free-silica is required to explain X-discontinuity observations (Chen et al., 2017). However the potential for a reduction of free-silica in recycled basalts after dehydration and alteration processes during subduction, has called into question whether enough silica would be present to produce X-discontinuity observations (Knapp et al., 2015). In the context of Hawaiian magmatism, however, it is important to note that geochemical studies have concluded that mafic lithologies that have not lost substantial SiO2 during subduction processes are present in the mantle source regions (Jackson et al., 2012).

Ballmer et al. (2013, 2015) explore the dynamical effects of a plume enriched by dense eclogitic compositions. Their study suggests that such material may only be transported to the upper mantle in the central and therefore hottest part of the plume. In the region between the coesite-stishovite transition and the olivine-wadsleyite transition (300-410 km), the eclogitic component is negatively buoyant, which causes ponding in this depth range, forming a so-called Deep Eclogitic Pool (DEP). When the eclogitic material crosses the stishovite-to-coesite phase transition, the material becomes positively buoyant again. The presence of hot material ponding in a DEP could explain the broad low velocity anomalies around these depths in the tomographic model of Cheng et al. (2015). The numerical study by Dannberg and Sobolev (2015) also finds that mantle plumes containing up to 15-20% recycled oceanic crust as eclogite cause broad-scale ponding in the upper mantle.

4.2.4. Synthetic exploration

We apply a simplified synthetic test to explore if a coesite-stishovite phase transition in a DEP can explain the observations seen here, specifically those in the region E where we see a strong X-discontinuity and disappearance of the 410. We compute impedance contrasts for the coesite-stishovite and olivine-wadsleyite phases in different fractions using BurnMan - a Python library used to calculate thermo-elastic properties of mantle minerals (Cottaar et al., 2014) - with the database of Stixrude and Lithgow-Bertelloni (2011) (which does not currently account for the possibility of silica reduction in basalt by dehydration processes (Knapp et al., 2015)). We create synthetic models by modifying the PREM velocity model (Dziewonski and Anderson, 1981) to accommodate the computed velocities and density jumps at their observed depths beneath Hawaii, while removing the original 220 and 410 discontinuities in PREM. With increasing basalt fraction, the impedance contrast for the X-discontinuity increases, while that for the 410 diminishes (Figure 7a). This is reflected in the synthetic RF depth stacks (Figure 7b and c) by a change in relative RF amplitudes for the different conversions. The stacks use the same distance distribution as the stacks for region E (Figure 6), but for each distance are stacked over different event depths (see Section 2.4). In the synthetics we see an increase in the amplitudes of the arrivals for higher frequencies, which is not reflected in the real data (Figure 6). This could be due to less coherent stacking of high-frequency arrivals in the real data, or the phase transitions occurring over a broader depth than has been modelled here. In general, given more incoherent stacking and noise in the data, around 60-70% basalt accumulation can explain the disappearing 410.

Both for the real data and synthetics it is easier to compare the amplitude of the multiple phase (PPvXs) rather than the direct phase (PXs) in slowness stacks as there are fewer interfering phases $\sim$100 seconds after the P wave. Synthetic slowness stacks are shown for 20% and 50% basalt for both filters in Figure 8. The observed relative amplitude of PPvXs is 2.0% for region E (Figure 6). In the synthetics, such amplitudes are reached when 40-50% basalt is included. Thus less basalt accumulation (40-50%) can explain the observations from the X-discontinuity at the top of the DEP, while stronger accumulation of basalt (60-70%) at the bottom of the DEP in region E is needed to explain the disappearing 410.

It should be stressed that the basalt component of 40-70% required across the DEP to explain both the X-discontinuity and the 410 cannot be carried up by a plume. The plume could carry a basaltic component of up to 20% (Ballmer et al., 2013, 2015; Dannberg and Sobolev, 2015) which would have to accumulate within the DEP to create higher percentages. Dynamical models that allow for segregation and accumulation of components have not been tested to our knowledge. Additionally, dynamical models would have to test if the DEP can expand laterally and to shallower depths to allow the coesite-stishovite to be visible over a broad area.

We note that the arrivals from the X-discontinuity in the synthetic slowness stacks do not capture the negative swing before these arrivals observed in data (e.g. around 30 seconds in Figure 6b). Creating synthetics with a negative velocity jump (i.e. the top of a lower velocity zone as invoked to explain similar observations in Huckfeldt et al. (2013)), did not recreate a strong amplitude multiple. We note that subtle changes in velocity model (i.e. a change in gradient) or broader discontinuities, can change the shape of the phase arrival in receiver functions. Exploring this space of velocity models is beyond the scope of this study.

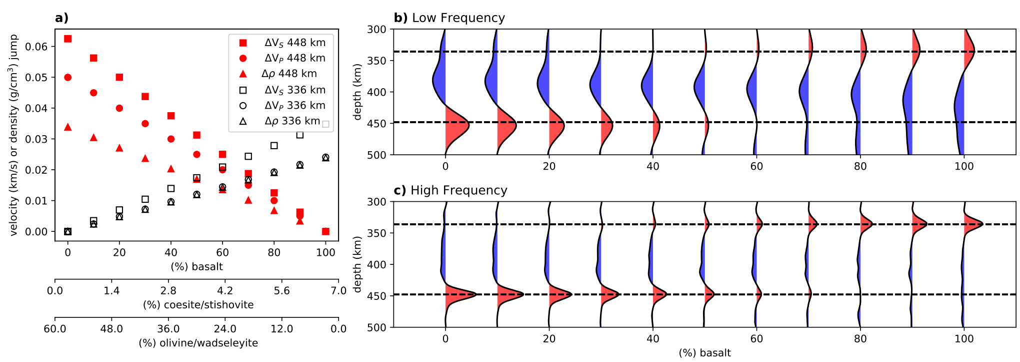

Figure 7: a) Predicted velocity and density jumps for a mechanical mixture of harzburgite and basalt. b) and c) Depths stacks for low -frequency (b) and high-frequency (c) synthetic receiver functions using predicted velocity and density jumps fixed at 336 km for the X-discontinuity and a gradual discontinuity from 443-453 km for the 410 for different basalt contents.

4.3. Summary of the plume across the upper mantle

We suggest the plume stem crosses the MTZ to the southwest of the Big Island (see cartoon in Figure 9), where its hot temperatures (200−300 K) thin the MTZ and lead to splitting of the 660 due to the presence of both an olivine and a majorite garnet transition. The plume carries recycled basaltic material which may act to enhance the garnet transition. As the

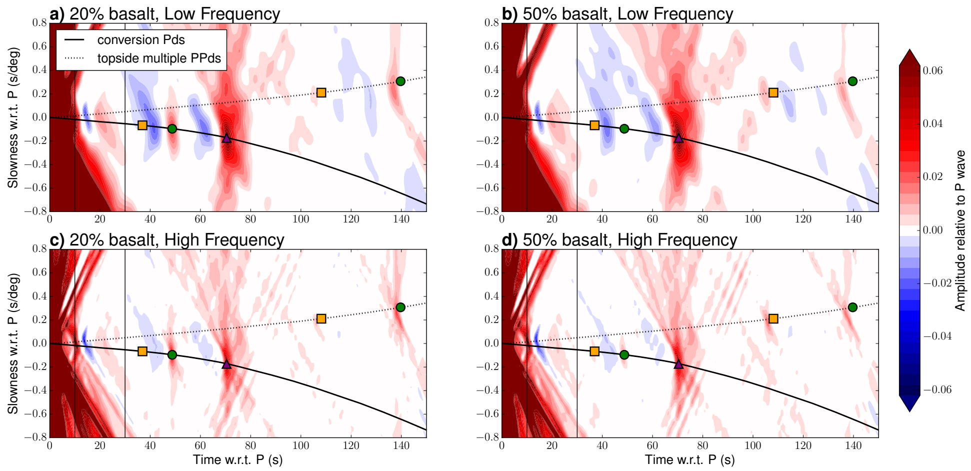

Figure 8: Slowness stacks (>2 SE) for synthetic receiver functions for a model with 20% basalt (a and c) and 50% basalt (b and d) at the Low (a and b) and High (c and d) frequency. Predicted lines for the conversion (solid) and multiple phases (dotted) in slowness/time space using PREM are shown as: Pds (direct conversion) - solid line, PPvds (multiple) - dashed line. Markers are shown for arrival times of Pds and PPvds phases from depths of 336 km (orange square), 448 km (green circle) and 670 km (purple triangle).

plume material crosses the 410 phase transition, it becomes less buoyant and starts to pond and spread out, creating a Deep Eclogitic Pool from 300-410 km (Ballmer et al., 2013). Spreading of the hot material in the DEP causes the 410 to appear depressed over a wide region and correlates with widespread slow velocities in the model of Cheng et al. (2015). The lack of an olivine phase transition at 410 km to the east of the Big Island could result from strong accumulation of basaltic material at the bottom of the DEP and sinking of the material into the transition zone. The presence of widespread basaltic material in the upper mantle is supported by the presence of the X-discontinuity, which can be related to the coesite-to-stishovite transition.

4.3.1. Connection to geochemical trends

The geochemistry of Hawaiian basalts implies spatial variation in the proportion of non-peridotitic material in their mantle source regions, showing an enhanced contribution of recycled material in the Loa chain in the SW as opposed to the Kea chain in the NE (e.g. Sobolev et al., 2005; Frey et al., 2016; Herzberg, 2010; Weis et al., 2011). A straightforward explanation for the distribution of these chains is that the mantle under the Loa-chain volcanoes contains a greater proportion of recycled mafic material, which may be present as eclogite at depth and react with surrounding peridotite to form pyroxenite beneath the SW Loa volcanoes. Our mapping of the X-discontinuity does not have the resolution to map variation in eclogite within the plume stem.

We do observe that the plume stem across the MTZ lies towards the southwest of the Big Island on the Loa side of the chain. While the plume is offset to directly beneath the Big Island across the DEP, the plume flux is likely higher closer to its source across the transition zone and could thus entrain more eclogitic material on the Loa-side as is shown in asymmetrical plume models (e.g. Ballmer et al., 2015). Seismic studies of the lithosphere find slower velocities (Laske et al., 2011) and deeper onset of melting (Rychert et al., 2013) on the Loa-side.

We note that in our observations, the strongest evidence of eclogite ponding (DEP) lies to the east, where the 410 dissappears, which is on the Kea-side. However, this observation does not have to have a direct relationship to the zonation of the plume-derived melts at the surface. To the east the DEP appears so enriched in eclogitic material that strong accumulations ($60-70\%$) are ponding and sinking into the transition zone (affecting the observations of 410 arrivals), hence the negative buoyancy of the accumulated material in the DEP might not allow entrainment of this material. The dynamical models of Ballmer et al. (2015) also show sinking of enriched material through the 410 away from the main plume stem.

It has also been suggested that the geochemical zonation is inherited by different entrained compositions from the lowermost mantle (e.g. Farnetani and Hofmann, 2010; Weis et al., 2011). Ballmer et al. (2013, 2015) shows that such zonation is not retained in the presence of a DEP.

Ballmer et al. (2015) argue for an alternative explanation where thermal asymmetry resulting from a model with a DEP can cause the observed trends when melting behaviour of the different lithologies is included in the geodynamical models. In these models the greatest relative contribution of fusible lithologies such as eclogite or pyroxenite is greatest in the cooler parts of the plume. In higher temperature parts of the planform the relative contribution from refractory lithologies, such as peridotite, is increasingly important. As such, the melting of lithologically heterogeneous mantle, temperature and not the amount of eclogite fed from the plume causes the variations in enrichment of basalt compositions. Hotter temperatures resulting in less enriched melt would argue for the Kea-side to be hotter, which is inconsistent with our observations of the plume crossing the MTZ closer to the Loa-side. Therefore, we suggest that it is entrainment processes, rather than the thermal nature of the plume, that limits the eclogite sourced on both sides of the plume to cause pyroxenite melts.

While the geodynamical models of Ballmer et al. (2013, 2015) and Dannberg and Sobolev (2015) show eclogite enrichment in the plume source has a great impact on plume dynamics and creation of a DEP, we do note that their models are limited by tracking two fixed compositions: enriched plume material (up to 16% eclogite) and surrounding peridotite. This model does not allow for further accumulation during the ponding of eclogite in the DEP, which is required to explain our observations. Therefore the models may not reflect the full complexities of variable entrainment of eclogite material out of the DEP, and this could be a motivation for further research.

5. Conclusion

We use 5132 high quality RFs to detect P-to-s conversions and associated multiples in order to image seismic discontinuities in the mid-to-upper mantle beneath the Hawaiian Islands. The RFs are stacked in a variety of ways to increase the signal-to-noise ratio, including depth stacks to define the depth of possible discontinuities, slowness stacks to distinguish between true conversions and multiples, and CCP stacks to investigate lateral variability.

We find lateral variations on three distinct discontinuities:

- Across the region we find the presence of an X-discontinuity around 290-350 km depth. While the direct arrival of this discontinuity (PXs)

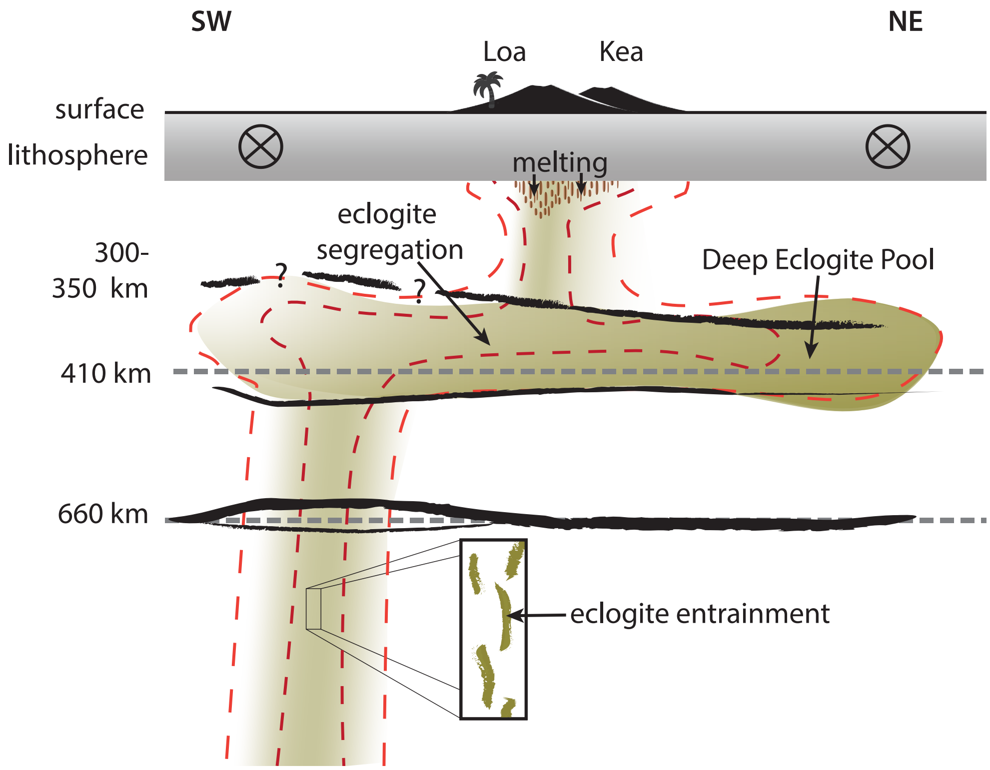

Figure 9: Summary cartoon. The hot mantle plume material (shown in a green-brown) upwells to 660 km in the SW where the 660 discontinuity appears split due to increased temperatures and basalt content. The 410 is depressed throughout the region below 410 km. There are patches of the X-discontinuity between 300-350 km throughout the region. The cartoon shows the hypothesised Deep Eclogite Pool which spreads above the 410 and could explain the presence of the X-discontinuity and the disappearance of the 410. The hot plume continues from the DEP up to the surface to cause the hotspot volcanism that created Hawaii.

interferes with a strong multiple from shallower depths, corroborative evidence of its presence comes from the observation of a multiple from this discontinuity (PPvXs).

- The 410 is depressed throughout the region by ~20 km. Additionally, the conversion from the 410 almost disappears to the east of the Big Island in conjunction with the strongest amplitude observations of the X-discontinuity.

- The 660 appears around 660 km depth across much of the region, except the area to the southwest of the Big Island. Here the 660 is split into a stronger arrival around 630 km and a weaker arrival around 700 km.

We hypothesise that southwest of the Big Island is the location where the hot, upwelling mantle plume crosses the 660. The high temperatures cause the dissociation reaction of ringwoodite to occur at shallower depths (thinning the MTZ), and garnet to be stable, causing a deeper garnet-controlled peak. More garnet can also be present due to an eclogitic component carried up in the plume.

In the upper mantle, we hypothesise ponding and accumulation of an eclogitic component. This would cause widespread hot temperatures, which would deepen the 410 across a wide area. Strong accumulation of eclogite on top of the 410 can also cause the observed disappearance of the 410 to the East of the Big Island. The stishovite component present in eclogite undergoes a conversion to coesite explaining the observed X-discontinuity across the region. The variability of geochemical trends observed in erupted lavas at the surface might be explained by increased entrainment of eclogite towards the SW where the plume may be hotter due to its proximity to the plume stem across the MTZ.

Acknowledgements

The authors would like to thank Kieran Gilmore, Annemijn van Stiphout and Simon Thomas for their contributions to the methods and Maxim Ballmer for discussions on the interpretation. This study uses Obspy (Krischer et al., 2015). Data is retrieved from IRIS DMC (www.iris.edu) from networks G [GEOSCOPE], GE [GEOFON], IU [Global Seismograph Network], YS [PLUME], HV [USGS Hawaiian Volcano Observatory (HVO)], XH [Hawaiian South Flank Slow EQ Project], XJ, and 9B. This work was supported by the Natural Environment Research Council [NERC grant reference number NE/R010862/1] and the Isaac Newton Trust. This project has also received funding from the European Research Council (ERC) under the European Unions Horizon 2020 research and innovation programme (grant agreement No. 804071 -ZoomDeep).

References

Agius, M.R., Rychert, C.A., Harmon, N., Laske, G., 2017. Mapping the mantle transition zone beneath Hawaii from Ps receiver functions: Evidence for a hot plume and cold mantle downwellings. Earth and Planetary Science Letters 474, 226–236. URL: `http://www.sciencedirect.com/science/article/pii/S0012821X17303497`, doi:`10.1016/j.epsl.2017.06.033`.

Akaogi, M., Akimoto, S.I., 1980. High-pressure stability of a dense hydrous magnesian silicate $Mg_{23}Si_8O_{42}H_6$ and some geophysical implications. Journal of Geophysical Research: Solid Earth 85, 6944–6948. URL: `https://agupubs.onlinelibrary.wiley.com/doi/abs/10.1029/JB085iB12p06944`, doi:`10.1029/JB085iB12p06944`.

Akaogi, M., Yusa, H., Shiraishi, K., Suzuki, T., 1995. Thermodynamic properties of -quartz, coesite, and stishovite and equilibrium phase relations at high pressures and high temperatures. Journal of Geophysical Research: Solid Earth 100, 22337–22347. URL: `https://agupubs.onlinelibrary.wiley.com/doi/abs/10.1029/95JB02395`, doi:`10.1029/95JB02395`.

Andrews, J., Deuss, A., 2008. Detailed nature of the 660 km region of the mantle from global receiver function data. Journal of Geophysical Research: Solid Earth 113. URL: `https://agupubs.onlinelibrary.wiley.com/doi/abs/10.1029/2007JB005111`, doi:`10.1029/2007JB005111`.

Audet, P., 2016. Receiver functions using OBS data: Promises and limitations from numerical modelling and examples from the cascadia initiative. Geophysical Journal International 205, 1740–1755.

Ballmer, M.D., Ito, G., Cheng, C., 2015. Asymmetric dynamical behavior of thermochemical plumes and implications for hawaiian lava composition. Hawaiian Volcanoes: From Source to Surface 208, 35.

Ballmer, M.D., Ito, G., Wolfe, C.J., Solomon, S.C., 2013. Double layering of a thermochemical plume in the upper mantle beneath Hawaii. Earth and Planetary Science Letters 376, 155–

164. URL: http://www.sciencedirect.com/science/article/pii/S0012821X13003385, doi:10.1016/j.epsl.2013.06.022.

Bastow, I.D., 2012. Relative arrival-time upper-mantle tomography and the elusive background mean. Geophysical Journal International 190, 1271–1278.

Chen, T., Gwanmesia, G.D., Wang, X., Zou, Y., Liebermann, R.C., Michaut, C., Li, B., 2015. Anomalous elastic properties of coesite at high pressure and implications for the upper mantle X-discontinuity. Earth and Planetary Science Letters 412, 42–51.

Chen, T., Liebermann, R.C., Zou, Y., Li, Y., Qi, X., Li, B., 2017. Tracking silica in earth's upper mantle using new sound velocity data for coesite to 5.8 GPa and 1073 K. Geophysical Research Letters 44, 7757–7765.

Cheng, C., Allen, R.M., Porritt, R.W., Ballmer, M.D., 2015. Seismic constraints on a double-layered asymmetric whole-mantle plume beneath Hawaii. John Wiley & Sons Inc., Hoboken, NJ.

Cottaar, S., Deuss, A., 2016. Large-scale mantle discontinuity topography beneath Europe: Signature of akimotoite in subducting slabs. Journal of Geophysical Research: Solid Earth 121, 279–292. URL: https://agupubs.onlinelibrary.wiley.com/doi/abs/10.1002/2015JB012452, doi:10.1002/2015JB012452.

Cottaar, S., Heister, T., Rose, I., Unterborn, C., 2014. BurnMan: A lower mantle mineral physics toolkit. Geochemistry, Geophysics, Geosystems 15, 1164–1179. URL: https://agupubs.onlinelibrary.wiley.com/doi/abs/10.1002/2013GC005122, doi:10.1002/2013GC005122.

Courtier, A.M., Bagley, B., Revenaugh, J., 2007. Whole mantle discontinuity structure beneath Hawaii. Geophysical Research Letters 34. URL: https://agupubs.onlinelibrary.wiley.com/doi/abs/10.1029/2007GL031006, doi:10.1029/2007GL031006.

Dannberg, J., Sobolev, S.V., 2015. Low-buoyancy thermochemical plumes resolve controversy of classical mantle plume concept. Nature Communications 6, 6960. URL: https://www.nature.com/articles/ncomms7960, doi:10.1038/ncomms7960.

Deuss, A., Woodhouse, J.H., 2002. A systematic search for mantle discontinuities using SS-precursors. Geophysical Research Letters 29, 90–1–90–4. URL: https://agupubs.onlinelibrary.wiley.com/doi/abs/10.1029/2002GL014768, doi:10.1029/2002GL014768.

Dziewonski, A.M., Anderson, D.L., 1981. Preliminary reference Earth model. Physics of the Earth and Planetary Interiors 25, 297–356. URL: http://www.sciencedirect.com/science/article/pii/0031920181900467, doi:10.1016/0031-9201(81)90046-7.

Eiler, J.M., Farley, K.A., Valley, J.W., Hofmann, A.W., Stolper, E.M., 1996. Oxygen isotope constraints on the sources of Hawaiian volcanism. Earth and Planetary Science Letters 144, 453–467. URL: http://www.sciencedirect.com/science/article/pii/S0012821X96001707, doi:10.1016/S0012-821X(96)00170-7.

Farnetani, C.G., Hofmann, A.W., 2010. Dynamics and internal structure of the Hawaiian plume. Earth and Planetary Science Letters 295, 231–240. URL: http://www.sciencedirect.com/science/article/pii/S0012821X10002396, doi:10.1016/j.epsl.2010.04.005.

French, S.W., Romanowicz, B., 2015. Broad plumes rooted at the base of the Earth's mantle beneath major hotspots. Nature 525, 95–99. URL: https://www.nature.com/articles/nature14876, doi:10.1038/nature14876.

Frey, F.A., Huang, S., Xu, G., Jochum, K.P., 2016. The geochemical components that distinguish Loa- and Kea-trend Hawaiian shield lavas. Geochimica et Cosmochimica Acta 185, 160–181. URL: http://www.sciencedirect.com/science/article/pii/S0016703716301697, doi:10.1016/j.gca.2016.04.010.

Fuchs, K., Müller, G., 1971. Computation of Synthetic Seismograms with the Reflectivity Method and Comparison with Observations. Geophysical Journal International 23, 417–433. URL: https://academic.oup.com/gji/article/23/4/417/583994, doi:10.1111/j.1365-246X.1971.tb01834.x.

Ganguly, J., Frost, D.J., 2006. Stability of anhydrous phase B: Experimental studies and implications for phase relations in subducting slab and the X discontinuity in the mantle. Journal of Geophysical Research: Solid Earth 111.

Garnero, E.J., McNamara, A.K., Shim, S.H., 2016. Continent-sized anomalous zones with low seismic velocity at the base of Earth's mantle. Nature Geoscience 9, 481–489. URL: https://www.nature.com/articles/ngeo2733, doi:10.1038/ngeo2733.

Hauri, E.H., 1996. Major-element variability in the Hawaiian mantle plume. Nature 382, 415–419. URL: https://www.nature.com/articles/382415a0, doi:10.1038/382415a0.

Herzberg, C., 2010. Identification of source lithology in the hawaiian and canary islands: Implications for origins. Journal of Petrology 52, 113–146.

Hirose, K., 2002. Phase transitions in pyrolitic mantle around 670-km depth: Implications for upwelling of plumes from the lower mantle. Journal of Geophysical Research: Solid Earth 107, ECV 3–1–ECV 3–13. URL: https://agupubs.onlinelibrary.wiley.com/doi/abs/10.1029/2001JB000597, doi:10.1029/2001JB000597.

Hofmann, A.W., White, W.M., 1982. Mantle plumes from ancient oceanic crust. Earth and Planetary Science Letters 57, 421–

436. URL: http://www.sciencedirect.com/science/article/pii/0012821X82901613, doi:10.1016/0012-821X(82)90161-3.

Huckfeldt, M., Courtier, A.M., Leahy, G.M., 2013. Implications for the origin of Hawaiian volcanism from a converted wave analysis of the mantle transition zone. Earth and Planetary Science Letters 373, 194–204. URL: http://www.sciencedirect.com/science/article/pii/S0012821X13002410, doi:10.1016/j.epsl.2013.05.003.

Ito, E., Takahashi, E., 1989. Postspinel transformations in the system Mg_2SiO_4-Fe_2SiO_4 and some geophysical implications. Journal of Geophysical Research: Solid Earth 94, 10637–10646. URL: https://agupubs.onlinelibrary.wiley.com/doi/abs/10.1029/JB094iB08p10637, doi:10.1029/JB094iB08p10637.

Jackson, M.G., Weis, D., Huang, S., 2012. Major element variations in hawaiian shield lavas: Source features and perspectives from global ocean island basalt (oib) systematics. Geochemistry, Geophysics, Geosystems 13.

Jenkins, J., Cottaar, S., White, R.S., Deuss, A., 2016. Depressed mantle discontinuities beneath Iceland: Evidence of a garnet controlled 660 km discontinuity? Earth and Planetary Science Letters 433, 159–168. URL: http://www.sciencedirect.com/science/article/pii/S0012821X15006895, doi:10.1016/j.epsl.2015.10.053.

Jenkins, J., Deuss, A., Cottaar, S., 2017. Converted phases from sharp 1000 km depth mid-mantle heterogeneity beneath Western Europe. Earth and Planetary Science Letters 459, 196–207. URL: http://www.sciencedirect.com/science/article/pii/S0012821X16306653, doi:10.1016/j.epsl.2016.11.031.

Jennings, E.S., Holland, T.J., 2015. A simple thermodynamic model for melting of peridotite in the system ncfmasocr. Journal of Petrology 56, 869–892.

Katsura, T., Ito, E., 1989. The system Mg_2SiO_4-Fe_2SiO_4 at high pressures and temperatures: Precise determination of stabilities of olivine, modified spinel, and spinel. Journal of Geophysical Research: Solid Earth 94, 15663–15670. URL: https://agupubs.onlinelibrary.wiley.com/doi/abs/10.1029/JB094iB11p15663, doi:10.1029/JB094iB11p15663.

Knapp, N., Woodland, A.B., Klimm, K., 2015. Experimental constraints on coesite abundances in eclogite and implications for the X seismic discontinuity. Journal of Geophysical Research: Solid Earth 120, 4917–4930.

Krischer, L., Megies, T., Barsch, R., Beyreuther, M., Lecocq, T., Caudron, C., Wassermann, J., 2015. Obspy: A bridge for seismology into the scientific python ecosystem. Computational Science & Discovery 8, 014003.

Laske, G., Collins, J.A., Wolfe, C.J., Solomon, S.C., Detrick, R.S., Orcutt, J.A., Bercovici, D., Hauri, E.H., 2009. Probing the Hawaiian Hot Spot With New Broadband Ocean Bottom Instruments. Eos, Transactions American Geophysical Union 90, 362–363. URL: http://onlinelibrary.wiley.com/doi/10.1029/2009EO410002/abstract, doi:10.1029/2009EO410002.

Laske, G., Markee, A., Orcutt, J.A., Wolfe, C.J., Collins, J.A., Solomon, S.C., Detrick, R.S., Bercovici, D., Hauri, E.H., 2011. Asymmetric shallow mantle structure beneath the hawaiian swell-evidence from rayleigh waves recorded by the plume network. Geophysical Journal International 187, 1725–1742.

Laske, G., Masters, G., Ma, Z., Pasyanos, M., 2013. Update on CRUST 1.0 − a 1-degree global model of Earths crust, in: Geophys. Res. Abstr, EGU General Assembly Vienna, Austria. p. 2658.

Lawrence, J.F., Shearer, P.M., 2006. A global study of transition zone thickness using receiver functions. Journal of Geophysical Research: Solid Earth 111. URL: https://agupubs.onlinelibrary.wiley.com/doi/abs/10.1029/2005JB003973, doi:10.1029/2005JB003973.

Li, X., Kind, R., Priestley, K., Sobolev, S.V., Tilmann, F., Yuan, X., Weber, M., 2000. Mapping the Hawaiian plume conduit with converted seismic waves. Nature 405, 938–941. URL: http://www.nature.com/nature/journal/v405/n6789/abs/405938a0.html, doi:10.1038/35016054.

Ligorra, J.P., Ammon, C.J., 1999. Iterative deconvolution and receiver-function estimation. Bulletin of the Seismological Society of America 89, 1395–1400. URL: http://www.bssaonline.org/content/89/5/1395.

Liu, H., Wang, W., Jia, X., Leng, W., Wu, Z., Sun, D., 2018. The combined effects of post-spinel and post-garnet phase transitions on mantle plume dynamics. Earth and Planetary Science Letters 496, 80–88. URL: http://www.sciencedirect.com/science/article/pii/S0012821X18303145, doi:10.1016/j.epsl.2018.05.031.

McDonough, W.F., Sun, S.S., 1995. The composition of the earth. Chemical geology 120, 223–253.

Rychert, C.A., Laske, G., Harmon, N., Shearer, P.M., 2013. Seismic imaging of melt in a displaced hawaiian plume. Nature Geoscience 6, 657.

Schmerr, N., 2015. Imaging mantle heterogeneity with upper mantle seismic discontinuities, in: Khan, A., Deschamps, F. (Eds.), The Earth's Heterogeneous Mantle: A Geophysical, Geodynamical, and Geochemical Perspective. Springer International Publishing, Cham. Springer Geophysics, pp. 79–104. URL: https://doi.org/10.1007/978-3-319-15627-9_3, doi:10.1007/978-3-319-15627-9_3.

Schmerr, N.C., Kelly, B.M., Thorne, M.S., 2013. Broadband array observations of the 300 km seismic discontinuity. Geophysical Research Letters 40, 841–846. URL: https://agupubs.onlinelibrary.wiley.com/doi/abs/10.1002/grl.50257, doi:10.1002/grl.50257.

Shen, Y., Wolfe, C.J., Solomon, S.C., 2003. Seismological evidence for a mid-mantle discontinuity beneath Hawaii and Iceland. Earth and Planetary Science Letters 214, 143–151. URL: http://www.sciencedirect.com/science/article/pii/S0012821X03003492, doi:10.1016/S0012-821X(03)00349-2.

Sobolev, A.V., Hofmann, A.W., Sobolev, S.V., Nikogosian, I.K., 2005. An olivine-free mantle source of Hawaiian shield basalts. Nature 434, 590–597. URL: https://www.nature.com/articles/nature03411, doi:10.1038/nature03411.

Stixrude, L., Lithgow-Bertelloni, C., 2011. Thermodynamics of mantle minerals - II. Phase equilibria. Geophysical Journal International 184, 1180–1213. URL: https://academic.oup.com/gji/article/184/3/1180/625783, doi:10.1111/j.1365-246X.2010.04890.x.

Weis, D., Garcia, M.O., Rhodes, J.M., Jellinek, M., Scoates, J.S., 2011. Role of the deep mantle in generating the compositional asymmetry of the Hawaiian mantle plume. Nature Geoscience 4, 831–838. URL: https://www.nature.com/articles/ngeo1328, doi:10.1038/ngeo1328.

Williams, Q., Revenaugh, J., 2005. Ancient subduction, mantle eclogite, and the 300 km seismic discontinuity. Geology 33, 1–4. URL: https://pubs.geoscienceworld.org/gsa/geology/article-abstract/33/1/1/129235/ancient-subduction-mantle-eclogite-and-the-300-km, doi:10.1130/G20968.1.

Wilson, J.T., 1963. A Possible Origin of the Hawaiian Islands. Canadian Journal of Physics 41, 863–870. URL: http://www.nrcresearchpress.com/doi/abs/10.1139/p63-094, doi:10.1139/p63-094.

Wölbern, I., Jacob, A.W.B., Blake, T.A., Kind, R., Li, X., Yuan, X., Duennebier, F., Weber, M., 2006. Deep origin of the Hawaiian tilted plume conduit derived from receiver functions. Geophysical Journal International 166, 767–781. URL: http://gji.oxfordjournals.org/content/166/2/767, doi:10.1111/j.1365-246X.2006.03036.x.

Woodland, A.B., 1998. The orthorhombic to high-P monoclinic phase transition in Mg-Fe Pyroxenes: Can it produce a seismic discontinuity? Geophysical Research Letters 25, 1241–1244. URL: https://agupubs.onlinelibrary.wiley.com/doi/abs/10.1029/98GL00857, doi:10.1029/98GL00857.

Xu, W., Lithgow-Bertelloni, C., Stixrude, L., Ritsema, J., 2008. The effect of bulk composition and temperature on mantle seismic structure. Earth and Planetary Science Letters 275, 70–79. URL: http://www.sciencedirect.com/science/article/pii/S0012821X08005281, doi:10.1016/j.epsl.2008.08.012.

Yu, C., Day, E.A., Maarten, V., Campillo, M., Goes, S., Blythe, R.A., van der Hilst, R.D., 2018. Compositional heterogeneity near the base of the mantle transition zone beneath hawaii. Nature communications 9, 1266.

Yu, Y.G., Wentzcovitch, R.M., Vinograd, V.L., Angel, R.J., 2011. Thermodynamic properties of $MgSiO_3$ majorite and phase transitions near 660 km depth in $MgSiO_3$ and Mg_2SiO_4: A first principles study. Journal of Geophysical Research: Solid Earth 116. URL: `https://agupubs.onlinelibrary.wiley.com/doi/abs/10.1029/2010JB007912`, doi:`10.1029/2010JB007912`.